

Chemistry

Special Topic: Chemistry Boosts Carbon Neutrality

CO₂-assisted formation of grain boundaries for efficient CO–CO coupling on a derived Cu catalyst

Zhuang-Zhuang Niu[#], Li-Ping Chi[#], Zhi-Zheng Wu, Peng-Peng Yang, Ming-Hui Fan & Min-Rui Gao^{*}*Division of Nanomaterials & Chemistry, Hefei National Laboratory for Physical Sciences at the Microscale, University of Science and Technology of China, Hefei 230026, China*[#]Contributed equally to this work.^{*}Corresponding author (email: mgao@ustc.edu.cn)

Received 5 September 2022; Revised 31 October 2022; Accepted 31 October 2022; Published online 17 February 2023

Abstract: The electrochemical CO₂ reduction reaction (CO₂RR) on Cu catalyst holds great promise for converting CO₂ into valuable multicarbon (C₂₊) compounds, but still suffers poor selectivity due to the sluggish kinetics of forming carbon–carbon (C–C) bonds. Here we reported a perovskite oxide-derived Cu catalyst with abundant grain boundaries for efficient C–C coupling. These grain boundaries are readily created from the structural reconstruction induced by CO₂-assisted La leaching. Using this defective catalyst, we achieved a maximum C₂₊ Faradaic efficiency of 80.3% with partial current density over 400 mA cm⁻² in neutral electrolyte in a flow-cell electrolyzer. By combining the structural and spectroscopic investigations, we uncovered that the *in-situ* generated defective sites trapped by grain boundaries enable favorable CO adsorption and thus promote C–C coupling kinetics for C₂₊ products formation. This work showcases the great potential of perovskite materials for efficient production of valuable multicarbon compounds via CO₂RR electrochemistry.

Keywords: electrochemical CO₂ reduction, multicarbon products, perovskite oxide, structural evolution, defective sites

INTRODUCTION

The electrochemical reduction of CO₂ (CO₂RR) into value-added fuels and chemical feedstock offers a sustainable route to store renewable electricity and to mitigate carbon emissions [1–7]. Currently, copper (Cu) is the most promising material capable of catalyzing C–C coupling to yield more valuable multicarbon (C₂₊) hydrocarbons and oxygenates [8,9]. However, a bulky flat Cu generally favors CH₄ production and generates significant amounts of H₂ from competitive hydrogen evolution reaction (HER), leading to unsatisfactory activity and selectivity for C₂₊ products [10,11]. To surmount this challenge, many strategies have been exploited to improve catalytic performance of Cu, including facet control [12], morphology manipulation [13], surface modification [14], and structural reconstruction [15,16]. Among these emerging strategies, structural reconstruction is of particular interest because it is expected to *in-situ* introduce structural defects such as vacancies [17], grain boundaries (GBs) [16], and dislocations [18], which contain rich undercoordinated sites and thus are believed to facilitate intermediates adsorption for catalyzing CO₂RR

efficiently [16,18–21]. However, designing advanced catalysts to achieve high-density defects via reconstruction and ultimately guide the reaction pathway remains challenging. This, to a great extent, is due to the limited investigations on the various catalysts and their reconstruction process [22].

Perovskite-type oxides possess flexible electronic structure and chemical versatility, which thus hold great potential to create highly active sites via structural reconstruction in the heterogeneous catalysis and electrocatalysis field. For example, derived Cu^+ sites anchored on $\text{LaMn}_{1-x}\text{Cu}_x\text{O}_3$ ($0.2 < x < 0.8$) matrix exhibited remarkable selectivity for catalyzing CO hydrogenation towards alcohols [23]. SrIrO_3 material has demonstrated the superior oxygen evolution reaction activity and stability in acidic electrolyte by *in-situ* forming the highly active IrO_x overlayer via Sr leaching [24]. Although intensive interest has been focused on the production of high-value multicarbon products from CO_2RR electrochemistry, the use of perovskite-type oxides-derived Cu as CO_2RR catalyst is rare, except for a few reports [25,26]. In 1993, Sammells and co-workers [25] employed perovskite-type $\text{La}_{1.8}\text{Sr}_{0.2}\text{CuO}_4$ to catalyze CO_2RR and achieved a ~40% Faradaic efficiency (FE) of alcohols at the total current density of 180 mA cm^{-2} in 0.5 M KOH using a gas diffusion electrode (GDE). Later, Yellowlees and co-workers [26] gained the 9.4% and 11.4% FEs towards ethylene and methane using the same catalyst. Although interesting, these prior work provided limited information regarding the structural evolution and real active site during electrolysis; moreover, the prospects of such materials for high-rate CO_2 conversion towards C_{2+} products are still unclear.

Herein, we report a La_2CuO_4 perovskite oxide-derived Cu (POD-Cu) catalyst rich in GBs. The high-density GBs were *in-situ* created in the structural reconstruction process induced by CO_2 -assisted La sites leaching. Using this GBs-rich Cu catalyst, we achieved a ~80.3% Faradaic efficiency towards C_{2+} products with partial current densities over 400 mA cm^{-2} in neutral environment in a flow-cell electrolyzer, outperforming the conventional CuO-derived Cu (OD-Cu) counterparts. By combining the structural and spectroscopic investigations, we uncovered that the introduction of high-density GBs enables abundant undercoordinated Cu sites and thus promote C–C coupling kinetics for C_{2+} products generation via enhancing CO intermediate adsorption. Our work highlights the great potential of Cu-based perovskite materials for efficient production of valuable multicarbon compounds via CO_2RR electrochemistry.

MATERIALS AND METHODS

For Cu-based perovskite oxides, the common materials are lanthanum cuprates with the general formula $\text{La}_{n+1}\text{Cu}_n\text{O}_{3n+1}$, which are well-known models for studying superconductivity phenomena in physics [27]. In this homologous series, La_2CuO_4 is considered to be the simplest member ($n=1$) [28], and recently exhibited electrocatalytic activity for some reduction reactions, such as oxygen reduction reaction and nitrate reduction reaction [29,30]. These advances have motivated us to choose La_2CuO_4 as an archetypal example of Cu-based perovskite to study its structural evolution and catalytic property in CO_2RR electrochemistry.

The La_2CuO_4 material was prepared by a sol-gel method. Briefly, 2.165 g $\text{La}(\text{NO}_3)_3 \cdot 6\text{H}_2\text{O}$, 0.582 g $\text{Cu}(\text{NO}_3)_2 \cdot 3\text{H}_2\text{O}$ and the complexing reagent citric acid monohydrate (1.576 g, equal to total metal ion molar concentration) were sequentially dissolved in deionized water in a glass beaker. The solution was concentrated with the evaporation of water by heating and became the viscous gel. Then the glass beaker containing viscous gel was placed in an oven kept at 200°C . The mixture underwent further dehydration

followed by decomposition with swelling and frothing, then ruptured with a flame, resulting in the voluminous and foamy precursor. By annealing the ground precursor powder at an optimized temperature of 700° C for 6 h in air (Figures S1–S3), followed by cooling in air, we gained the reddish brown La_2CuO_4 powder. More details can be found in the Supplementary Information.

RESULTS AND DISCUSSION

We performed X-ray diffraction (XRD) measurement of the obtained powder. As shown in Figure 1A, all of the diffraction peaks match well with orthorhombic-type perovskites structure of La_2CuO_4 , suggesting the absence of impurity in the sample. Figure 1B displays X-ray photoelectron spectroscopy (XPS) result of the La 3d and Cu 2p binding energy region. La 3d region shows the double peak structure of each spin-orbit split component with configurations of $3d^94f_0L$ and $3d^94f_1L$ (L denotes the oxygen ligand), which is typical of La^{3+} compounds [31]. Generally, the f_0 and f_1 separately dominate the low binding energy band and the high binding energy band. The f_1 - f_0 energy separations are characteristic of different La compounds, such as 3.9 eV for $\text{La}(\text{OH})_3$ [32], 4.3 eV for LaCoO_3 [31]. The value (3.2 eV) of the f_1 - f_0 energy separation here is similar to that reported (3.1 eV) for La_2CuO_4 [33]. The Cu 2p spectrum exhibits satellite peaks, which are characteristic of Cu^{2+} compounds, corresponding to the divalent Cu sites in the La_2CuO_4 perovskite structure. Scanning electron microscopy (SEM) and transmission electron microscopy (TEM) images of La_2CuO_4 show a porous worm-like nanostructures consisting of interconnected nanoparticles with an average diameter of about 50–200 nm (Figure 1C and Figure S4). The high resolution-transmission electron microscopy (HR-TEM) and selected-area electron diffraction (SAED) pattern uncover that the single nanoparticle is single crystal and is interconnected through distinct grain boundaries (Figure S4). Energy dispersive X-ray (EDX) spectrum elemental mapping in Figure 1D exhibits a uniform spatial distribution of La, Cu, and O elements in the sample. We further studied the detailed atomic structure of the La_2CuO_4 by aberration corrected high-angle annular dark-field scanning transmission electron microscopy (HAADF-STEM). The atomic-resolution Z-contrast images in Figure 1E clearly reveal an adjacent layered structures with different layer spacing of 3.4 and 2.8 Å respectively, where La atoms exhibit higher image intensity compared with Cu atoms. Using image contrast, the La and Cu atoms can be further identified by the line intensity profile (inset of Figure 1E) acquired along the yellow arrow of [001] direction. This result is consistent with the investigation that La_2CuO_4 is a kind of K_2NiF_4 -type structure consisting of alternate stackings of perovskite and rock salt blocks [34], where CuO_2 planes are separated by LaO-LaO rock-salt layers, forming the corner-shared CuO_6 octahedra as shown in Figure 1F.

Altogether, multiple characterizations above show that high-quality La_2CuO_4 perovskite was successfully synthesized by a simple sol-gel synthetic strategy. Additionally, this approach is scalable, which enables the production of high-yield La_2CuO_4 powders (>15 g one batch) with good fidelity for potential large-scale use (Figure S5). For a fair catalytic performance comparison, we also synthesized high-purity CuO powders by the same synthetic protocol without the addition of La. The obtained samples are mainly composed of irregular gravel-like particles with an average diameter of less than 200 nm (Figures S6 and S7).

To gain OD-Cu and POD-Cu electrocatalysts, the CuO and La_2CuO_4 -coated GDEs (with a catalyst loading of $\sim 1.0 \text{ mg cm}^{-2}$) were firstly activated through *in-situ* electrochemical reduction at a constant potential of

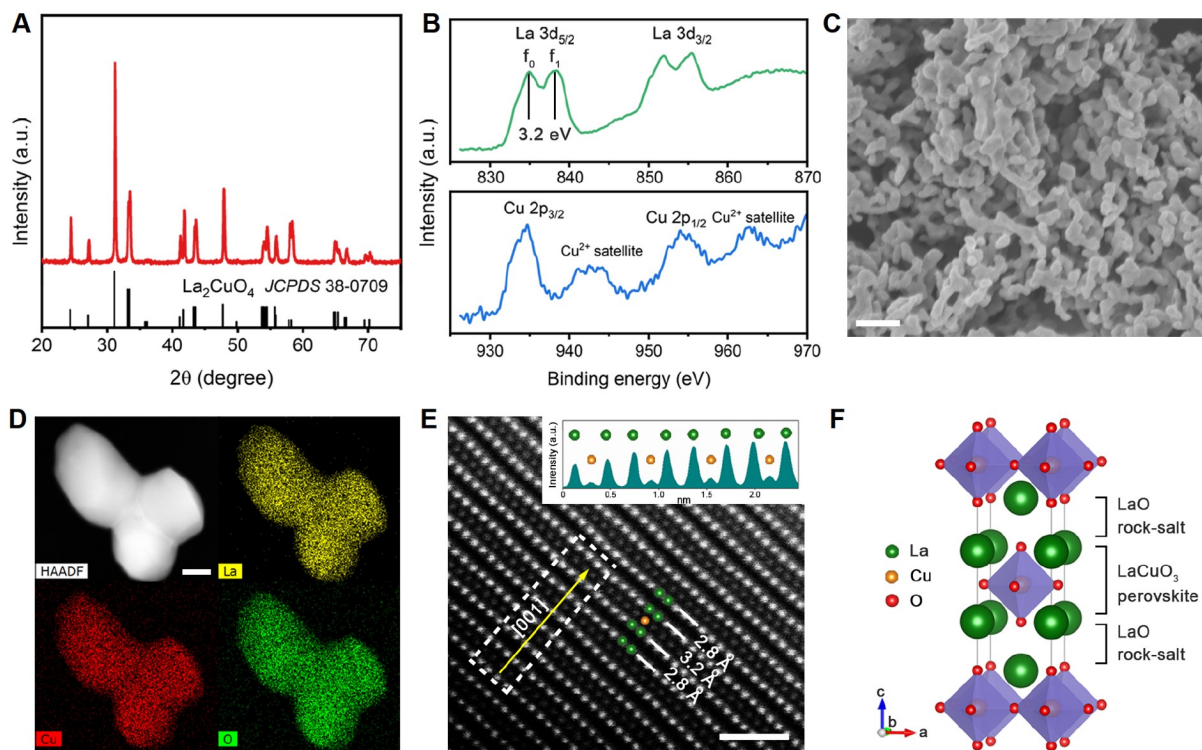


Figure 1 Physical characterization of La_2CuO_4 perovskite oxide. (A) XRD pattern of La_2CuO_4 powder. (B) XPS high resolution spectrum of the La 3d and Cu 2p region. (C) SEM image of La_2CuO_4 particle. Scale bar: 500 nm. (D) HAADF-STEM image and the corresponding EDS elemental mapping of La_2CuO_4 particle. Scale bar: 50 nm. (E) Atomic-resolution HAADF-STEM image of La_2CuO_4 . Scale bar: 1 nm. Inset is the line intensity profile acquired along the yellow arrow of [001] direction. Green and yellow balls represent La and Cu atoms, respectively. (F) Crystal structure of La_2CuO_4 .

−1.8 V (versus normal hydrogen electrode (NHE)) for 15 min in a three-compartment flow-cell setup (Figure S8). Interestingly, unlike CuO electrode that can be easily reduced to metallic Cu regardless of the atmosphere (Figure S9), the structural evolution of La_2CuO_4 perovskite during electrochemical process exhibits a strong atmosphere-dependent behavior. In Ar-saturated KCl, no obvious changes in the structure and morphology of La_2CuO_4 were observed after electrochemical activation (Figure 2A and Figure S10), indicating that La_2CuO_4 perovskite is hardly reducible under this condition, consistent with previous reports [30,35]. By contrast, when the electrolyte was aerated with CO_2 , we found that La element was progressively leached into the electrolyte during the activation process, confirmed by inductively coupled plasma atomic emission spectroscopy (ICP-AES, Figure S11). Consequently, the electrode was evolved from La_2CuO_4 perovskite structure into cubic Cu phase, as suggested by XPD pattern in Figure 2A.

The above results reveal that CO_2 plays a unique and important role in the evolution of La_2CuO_4 perovskite during electrochemical process, which can be reasonably explained by the following reasons. Under negative bias, a small amount of Cu sites on Cu-terminated surface of La_2CuO_4 are firstly reduced with the concomitant formation of La oxides regardless of in the Ar or CO_2 -feed catholyte [35]. In Ar-feed electrolyte, due to the extremely negative reduction potential of La oxides ($\ll -2.9$ V versus standard hydrogen electrode (SHE) [36]), the internal Cu sites of perovskite are blocked by La-O cages, thus preventing from being exsolved [37]. As a result, O vacancies may be created on the perovskite surface, and no significant

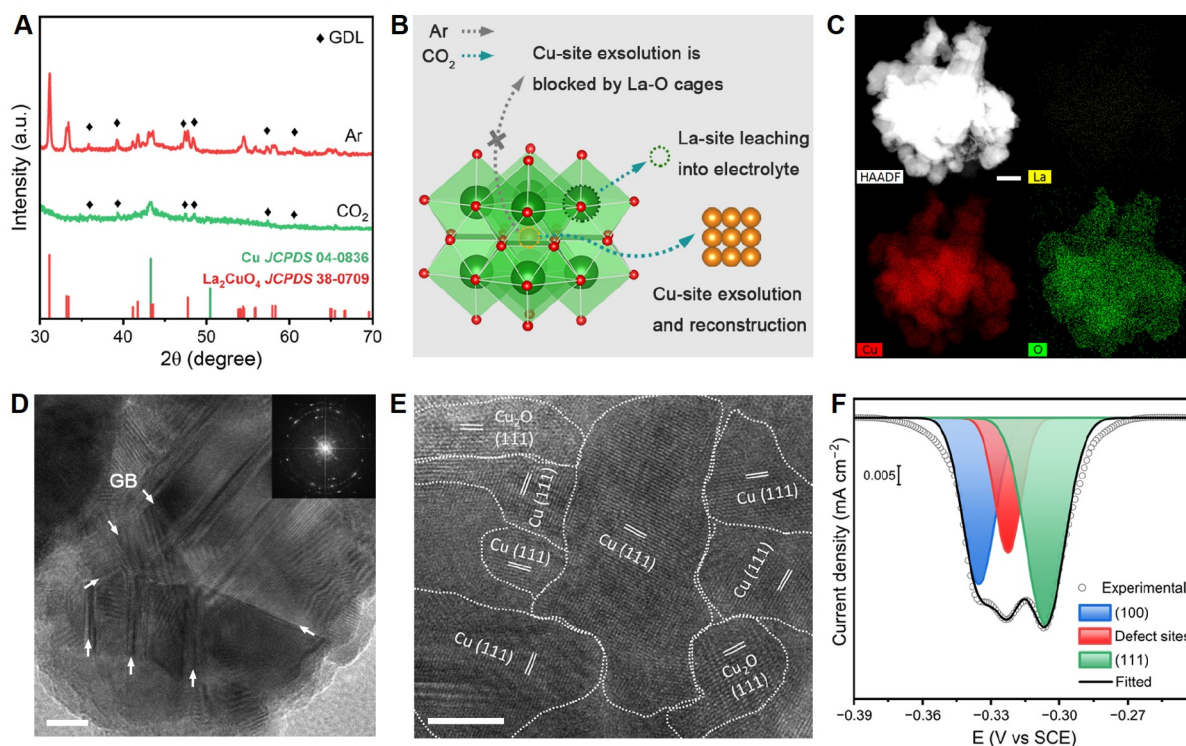


Figure 2 Physical characterization of POD-Cu. (A) XRD patterns of La₂CuO₄ electrodes after activation in Ar and CO₂-feed catholyte. The diffraction peaks marked by black rhombus originated from GDL substrate. The weak Cu diffraction in XRD pattern was the result of the very low content of Cu on the GDL (about 0.16 mg cm⁻¹). (B) Schematic diagram of the structural evolution of La₂CuO₄. (C) HAADF-STEM image and the corresponding EDX elemental mapping of POD-Cu. Scale bar: 100 nm. (D), (E) HR-TEM images of POD-Cu. Inset in (D) is the corresponding FFT pattern. Scale bars: 10 nm in (D) and 5 nm in (E). (F) Pb UPD profile of POD-Cu.

restructuring occurs [35]. When introducing CO₂ into the system, however, La oxides can react with CO₂ and H₂O to form La₂(CO₃)₃, which would be dissolved into the electrolyte by forming complex with carbonates generated in HER or CO₂RR process [38]. Accordingly, the leaching of La sites further leads to deep exsolution and reorganization of internal Cu sites, resulting in the collapse of perovskite structure with the concomitant formation of the metallic Cu phase, as illustrated in Figure 2B.

To gain the detailed structural information, we characterized the POD-Cu catalyst by multiple techniques. EDX elemental mapping measurements of randomly selected regions permit a quantitative analysis of composition at a relatively large scale. As displayed in Figure 2C and Figures S12 and S13, the atomic percentages of lanthanum are generally less than 0.15%, a value comparable to the detection limit of the instrument (about 0.1%), which suggest a complete leaching of La element during *in-situ* electrochemical activation process. Additionally, EDX elemental mapping and XPS spectrum (Figure S14) exhibited a thin oxide layer on the POD-Cu surface, originating from natural oxidation of nanostructured Cu exposed in the air. By combining XRD and EDX results, we determined a thoroughly structural transition from layer perovskite oxide to metallic Cu without residual La after the activation process. Correspondingly, the worm-like nanostructures of La₂CuO₄ reorganize into rougher multiparticles (Figure S15).

HR-TEM image (Figure 2D) shows that POD-Cu catalyst appeared as irregular aggregates, which are compactly composed of multiple nanocrystallites interconnected by distinct GBs (marked by white arrows),

corresponding to the polycrystalline diffraction rings in fast Fourier transform (FFT) pattern. Such single-to-polycrystalline transformation revealed that the initial La_2CuO_4 single crystals are fragmented into nanosized Cu grains connected each other during the activation process, which are more noticeable in the enlarged HR-TEM images (Figure 2E and Figure S16), thus resulting in high-density GBs. We highlight that these GBs can kinetically trap and stabilize lattice dislocations and deformations in polycrystalline materials, providing a way to create high-energy surfaces with abundant undercoordinated sites, i.e. GBs effects, as previously demonstrated by Kanan group [39,40]. Unlike POD-Cu catalyst, we identified that OD-Cu sample mainly presents continuous and regular lattice fringes in the microscopic analysis of multiple regions (Figures S17 and S18), indicating much fewer GBs and defective sites.

To obtain more insights into surface properties of the POD-Cu electrode, we employed highly sensitive Pb underpotential deposition (UPD) technique to probe the distribution of crystallographic domains on the catalyst surface (Figure S19). The UPD profile of POD-Cu in Figure 2F displays three overlapped voltammetric peaks in the potential window of -0.27 to -0.36 V versus saturated calomel electrode (SCE). According to previous reports on the Cu disk [41], these peaks are characteristic to Cu (111) facet, Cu (100) facet and defective sites respectively. The surface charge value of each peak was then obtained by integrating the deconvoluted peak after subtracting the base line that corresponds to the capacitive charge. We observe that the $\langle 111 \rangle$ and $\langle 100 \rangle$ domains are the predominant orientation on the POD-Cu surface, respectively, which contribute to 47% and 32% of the total surface charge (Table S1). Notably, the defective sites contribute to the total surface charge up to 20.9%, far exceeding that of 3.2% for OD-Cu. Based on the microscopic analysis and surface-sensitive probe measurement, we unveil that compared to OD-Cu, POD-Cu possesses abundant structural defects mainly trapped in high-density GBs. We reasonably attribute the defect-site-rich surface of POD-Cu to the dramatic collapse of perovskite structure that induced by the La sites leaching, as well as the exsolution and rearrangement of Cu sites.

We evaluated the CO_2RR catalytic properties of POD-Cu and OD-Cu electrodes using the same three-compartment flow-cell setup. We used neutral KCl (1 M, pH ~ 6.5) electrolyte as catholyte to mitigate (bi) carbonate issues [42]. The low buffering capability of the KCl electrolyte allows surface pH of the electrode to increase to a weakly basic range, which benefits C_{2+} production via positively shifting the C_{2+} onset potential and suppressing HER, as described by previous studies [43,44]. Considering that the electrode surface pH is substantially higher than the bulk pH during high-rate electrolysis in the non-buffering catholyte, all potentials are converted into the NHE rather than RHE scale to facilitate performance comparison on an absolute scale [43,45,46]. Gas-phase and liquid-phase products were quantified by gas chromatography (GC) and nuclear magnetic resonance (NMR) spectroscopy, respectively. Detailed information regarding the CO_2RR measurement is provided in the Supplementary Information.

Multiple products were detected from the CO_2RR on two Cu electrodes, including C_1 compounds (CO , formate and CH_4) and C_{2+} compounds (ethylene, ethanol, acetate and *n*-propanol). The FEs of different products yielded on POD-Cu and OD-Cu are summarized in Figure 3A and Tables S2 and S3. Initially, POD-Cu electrode exhibits a C_{2+} FE of $\sim 46\%$ at -1.67 V. As the potential shifts negatively, this FE value rapidly reaches $\sim 70\%$ at -2.12 V. Correspondingly, the FE of C_1 products, especially CO , significantly drops, suggesting the promoted C–C coupling kinetics for the formation of C_{2+} products. Intriguingly, the POD-Cu catalyst holds the high C_{2+} FE of over 70% in a broad potential range of ≤ -2.12 V. A maximal C_{2+} FE of 80.3% is achieved at -2.34 V, corresponding to 38.3% ethylene, 30.1% ethanol, 10.1% acetate, and 1.8%

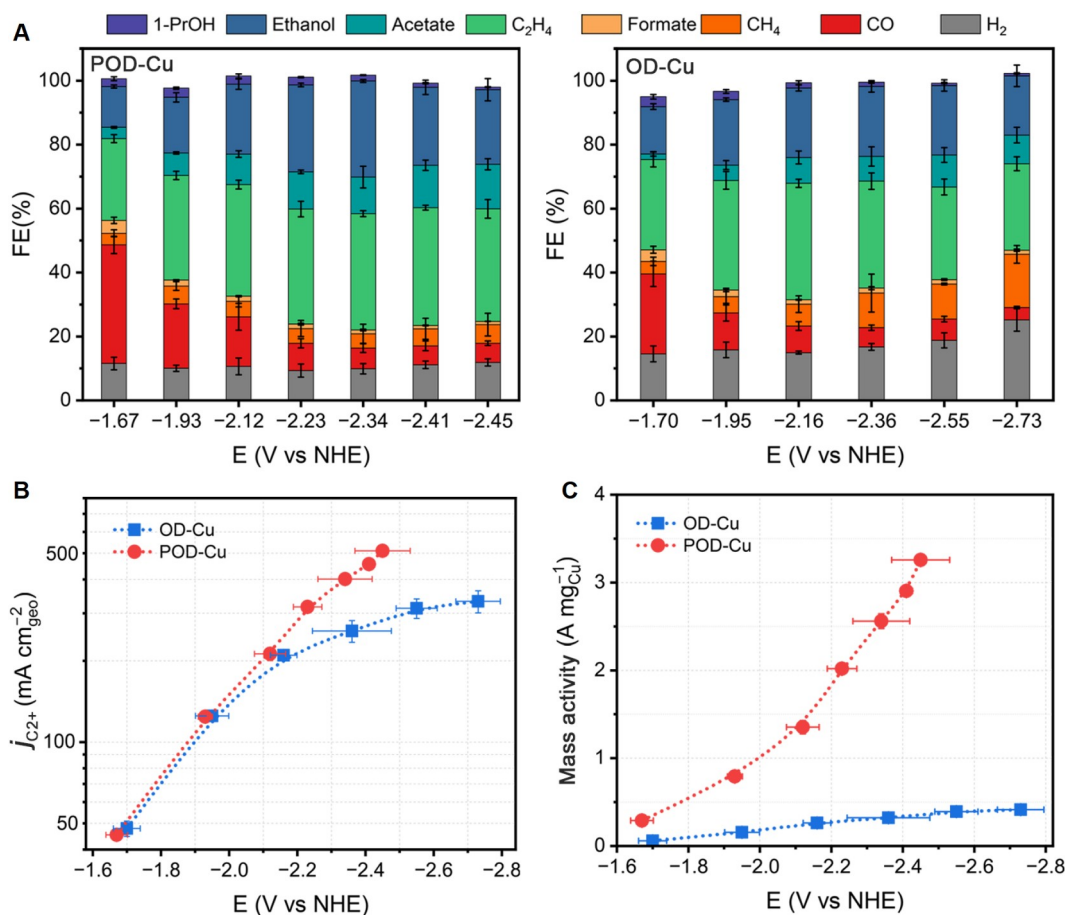


Figure 3 CO₂RR performance. (A) Faradaic efficiencies, (B) geometric current densities and (C) mass activities of C₂₊ products on POD-Cu and OD-Cu catalyst at various potentials. Error bars are based on the standard deviation of at least three independent measurements, and points are average values.

n-propanol, which is among the best CO₂RR performance in neutral electrolytes (Table S4). By contrast, the OD-Cu catalyst bears a lower C₂₊ FE less than 70% (Figure 3A) in the similar potential range, which agrees with previous reports on the OD-Cu catalysts [43,47,48]. In addition, compared with OD-Cu, POD-Cu exhibits lower H₂ selectivity (FE ≤ 12%, Figure 3A) and generation rate in the whole potential range (Figure S20), demonstrating that the competitive HER reaction was suppressed over the POD-Cu surface.

We also compared geometric current densities for C₂₊ production of two studied Cu catalysts at various applied potentials (Figure 3B). For POD-Cu electrode, there was a near-exponential increase of the C₂₊ current density in the whole potential range, indicating excellent C₂₊ generation rate with roughly stable selectivity even under high overpotentials. Impressively, the POD-Cu possesses a high C₂₊ current density of 511 mA cm⁻² at -2.45 V, holding promise to operate at industrial electrolyzer-relevant current densities. By contrast, the C₂₊ partial current density on OD-Cu increases exponentially only at low overpotentials and then turns to a near linear increase at high overpotentials. The limited C₂₊ products formation rate on OD-Cu is mainly caused by substantial generation of competitive H₂ and CH₄ under high overpotentials (Figure 3A). As a result, OD-Cu electrode only offered a C₂₊ partial current density of 332 mA cm⁻² even applying a more negative potential of -2.73 V. We further normalized the C₂₊ partial current density by electrochemically

active surface area (ECSA) gained from Pb UPD profile. ECSA-normalized C_{2+} partial current densities of POD-Cu electrode largely exceed that of OD-Cu at various studied potentials (Figure S21), indicating its superior intrinsic activity for C_{2+} production.

We highlight that the content of Cu element in La_2CuO_4 is much lower than that in CuO (0.16 mg cm^{-2} versus 0.80 mg cm^{-2}) under the same loading on GDE (typically 1 mg cm^{-2}), suggesting that the catalytic activity with respect to catalyst loading, i.e. the Cu mass activity, of the POD-Cu catalyst is higher. Indeed, Figure 3C shows that the C_{2+} mass activity of POD-Cu overwhelmingly outperforms OD-Cu at all potentials examined. In particular, POD-Cu possesses an outstanding mass activity of $\sim 3.26 \text{ A mg}_{Cu}^{-1}$ at -2.45 V , which represents the best mass activities observed on Cu-based catalysts for C_{2+} compounds (Table S4). The ultra-high mass activity of POD-Cu can be ascribed to small grain size, fully exposed surface and superior intrinsic activity.

Now, we turn to assess the long-term stability of our POD-Cu catalyst. To this end, we operated a continuous CO_2 electrolysis under a constant current density of 300 mA cm^{-2} in the flow-cell electrolyzer. A stable C_{2+} FE of 70%–75% was recorded during the 4-h continuous operation. The slight decrease in C_{2+} Faradaic efficiency later was predominantly due to the electrolyte flooding caused by the reduced hydrophobicity of the GDL (inset in Figure S22), thus leading to the CO_2 diffusion toward the catalyst layer to be blocked [49–52]. Post-mortem characterizations reveal that the abundant GBs are largely maintained (Figure S23), confirming the good operational stability of the defective catalyst.

For the CO_2RR on the Cu surface, adsorbed CO (CO_{ad}) is an essential intermediate towards the formation of multicarbon products. Prior studies have showed that the $C\equiv O$ stretch mode is highly sensitive to the applied potential, surface morphology and reaction site of catalysts [53]. Therefore, CO_{ad} becomes a powerful and broadly applicable spectroscopic probe of the electrochemical interface. We thus performed *in-situ* surface enhanced Raman spectroscopy (SERS, Figure S24) to exploit the utility of CO_{ad} probe to study the electrochemical interface of POD-Cu electrode.

Figure 4A exhibits the time-dependent SERS spectra in the range of $C\equiv O$ stretch mode during La_2CuO_4 activation process under the bias of -1.8 V . At 2 min, a band centered at $\sim 1820 \text{ cm}^{-1}$ and additional broad band in $1900\text{--}2100 \text{ cm}^{-1}$ emerge, which are assigned as bridge-bound CO (CO_{bridge}) and atop-bound CO (CO_{atop}), respectively. The SERS results here imply that the Cu sites in perovskite underwent exsolution and reorganized into the metallic Cu phase (Figure S25). We found that the CO_{bridge} band is dominantly present in the first 4 min, then the CO_{atop} band develops into a prominent feature in the following 10 min. The conversion of CO_{ad} configuration suggests that two distinct active sites were formed during the reconstruction process [54]. Generally, CO_{bridge} behaves relatively inert without participating in further C–C coupling step for yielding multicarbon products [55]. Instead, it is more likely an on-pathway intermediate in favor of CH_4 generation [56]. Indeed, product measurement during the *in-situ* electrochemical activation of La_2CuO_4 displayed a high CH_4 FE of $\sim 35\%$ in the first 10 min, but the value rapidly dropped to $\sim 7\%$ and C_2H_4 FE sharply increased from 6% to 37% in the following 10 min (Figure S26). Combining spectroscopic observation and experimental results, we conclude that at a negative bias, La_2CuO_4 perovskite first evolved into dispersed Cu particles supported on perovskite matrix, which prefer CO_{bridge} and generate CH_4 as the dominant product [57]. With deeper exsolution and reorganization of internal Cu sites, the perovskite oxide eventually transformed into Cu aggregates that favors CO_{atop} and promotes the formation of multicarbon products.

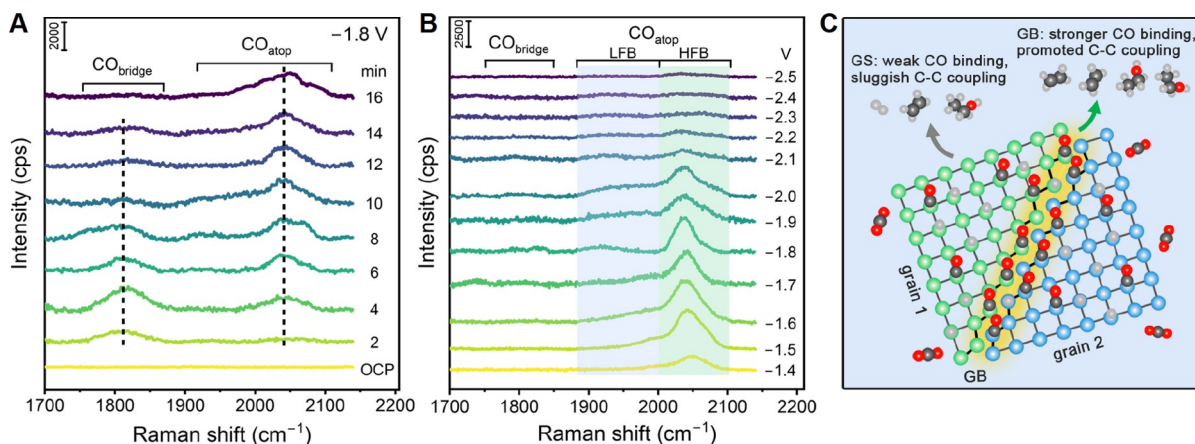


Figure 4 *In-situ* SERS spectra studies. (A) Time-dependent SERS spectra collected during the perovskite activation process at -1.8 V. (B) Potential-dependent SERS spectra of POD-Cu catalyst during CO₂RR. (C) Diagram of structure-activity relationship on POD-Cu surface. The green, blue balls represent Cu atoms in grain 1 and 2, and the black, red, gray balls represent C, O and H atoms, respectively.

Potential-dependent SERS spectra of POD-Cu catalyst were also collected, as shown in Figure 4B. Clearly, relatively inert CO_{bridge} band is very weak that can be ignored. By contrast, the reactive CO_{atop} is exclusively present at studied potentials, consistent with experimental results demonstrated in Figure 3A. Overall, at a lower overpotential range, the CO_{atop} band intensity raises with the increased CO coverage. At higher overpotentials, however, the fast consumption of CO_{ad} populations via deeper reduction leads to the declining of CO_{atop} band intensity. Moreover, CO_{ad} band typically consists of a low frequency band (LFB) centered at ~ 1960 cm⁻¹ and a high frequency band (HFB) centered at ~ 2040 cm⁻¹ (Figure S27).

Previous studies have well established that CO_{ad} binds on defective Cu sites more strongly, resulting in a blue-shift of the C≡O vibrational frequency of CO_{ad} [58]. This is because the electronic charge distribution at undercoordinated defects is significantly different from that at flat terraces (so-called Smoluchowski effect [59]). The reduced charge density at defects sites could lead to a reduction in repulsion between CO_{ad} molecules, thus giving rise to an increase of the CO binding intensity. Therefore, the LFB and HFE here are associated with CO_{atop} on terrace and defective sites, respectively. Due to dynamic dipole coupling effect of CO_{ad}, the HFB is amplified by intensity transfer from the LFB mode to the HFB mode, failing to quantify the ratio of these two sites [53]. Nonetheless, the apparent HFB on POD-Cu reveals the rich defective sites on the surface, mainly from GBs-trapped lattice dislocations and deformations [39,40], consistent with HR-TEM and Pb UPD analysis demonstrated above. In contrast to POD-Cu, OD-Cu surface mainly exhibits LFB (Figure S28), suggesting limited defective sites on its surface and thus weaker CO_{atop} binding strength.

For the formation of multicarbon products, suitably high CO binding energy on the Cu surface is necessary so that the CO_{ad} can participate in further C–C coupling step before desorption. Compared with terrace sites, defective sites typically bind CO more strongly by about 50–100 meV [60,61]. Accordingly, they are predicted to give orders of magnitude higher reaction rates in CO₂RR than terrace sites because of the more favorable CO adsorption [62]. On the basis of the above analysis, we therefore attribute the excellent catalytic activity of POD-Cu to abundant defective sites, which are trapped and stabilized by the high-density GBs created from structural reconstruction. Compared with the terrace sites on grain surface (GS), these defective sites can bind the reactive CO_{atop} intermediates stronger, which not only promoted the possibility of di-

merization of neighboring CO_{atop} species but also largely suppressed H₂ evolution by limiting the access of *H intermediate to active sites.

CONCLUSIONS

In summary, the work reported here showcases a La₂CuO₄ perovskite oxide-derived Cu catalyst for electrochemical conversion of CO₂ into C₂₊ products in neutral environment with excellent selectivity and activity. A maximum C₂₊ FE of 80.3% and with C₂₊ partial current density beyond 400 mA cm⁻² was achieved, far outperforming the CuO-derived Cu counterparts. Structural characterizations and *in-situ* spectroscopic investigations revealed that the perovskite oxide-derived Cu possesses high-density grain boundaries containing abundant defective sites, which facilitate the C–C coupling step for C₂₊ products generation via enhancing the adsorption of key CO intermediates. We anticipate that our finding will find immediate use in the design of next generation CO₂RR catalysts based on flexible and efficient perovskite materials, which should aid the large-scale production of valuable C₂₊ compounds via CO₂RR electrochemistry.

Data availability

The original data are available from corresponding authors upon reasonable request.

Acknowledgements

We are grateful to Dr. Ming Zuo for his help in collecting the HRTEM data.

Funding

This work was supported by the National Basic Research Program of China (2018YFA0702001), the National Natural Science Foundation of China (21975237 and 51702312), Anhui Provincial Research and Development Program (202004a05020073), the USTC Research Funds of the Double First-Class Initiative (YD2340002007), the Fundamental Research Funds for the Central Universities (WK2340000101), the Technical Talent Promotion Plan (TS2021002), and the Recruitment Program of Global Youth Experts.

Author contributions

M.R.G. conceived and supervised the project. Z.Z.N. and L.P.C. performed the experiments, collected and analyzed the data. P.P.Y., Z.Z.W., and M.H.F. helped with material characterization and analysis. M.R.G. and Z.Z.N. co-wrote the manuscript. All authors discussed the results and commented on the manuscript.

Conflict of interest

The authors declare no conflict of interest.

Supplementary information

The supporting information is available online at <https://doi.org/10.1360/nso/20220044>. The supporting materials are published as submitted, without typesetting or editing. The responsibility for scientific accuracy and content remains entirely with the authors.

References

- 1 Artz J, Müller TE, Thenert K, *et al.* Sustainable conversion of carbon dioxide: An integrated review of catalysis and life cycle assessment. *Chem Rev* 2018; **118**: 434–504.
- 2 De Luna P, Hahn C, Higgins D, *et al.* What would it take for renewably powered electrosynthesis to displace petrochemical processes? *Science* 2019; **364**: aav3506.
- 3 Navarro-Jaén S, Virginie M, Bonin J, *et al.* Highlights and challenges in the selective reduction of carbon dioxide to methanol. *Nat Rev Chem* 2021; **5**: 564–579.
- 4 Wang G, Chen J, Ding Y, *et al.* Electrocatalysis for CO₂ conversion: From fundamentals to value-added products. *Chem Soc Rev* 2021; **50**: 4993–5061.
- 5 Li L, Li X, Sun Y, *et al.* Rational design of electrocatalytic carbon dioxide reduction for a zero-carbon network. *Chem Soc Rev* 2022; **51**: 1234–1252.
- 6 Kou Z, Li X, Wang T, *et al.* Fundamentals, on-going advances and challenges of electrochemical carbon dioxide reduction. *Electrochem Energy Rev* 2022; **5**: 82–111.
- 7 He J, Li Y, Huang A, *et al.* Electrolyzer and catalysts design from carbon dioxide to carbon monoxide electrochemical reduction. *Electrochem Energy Rev* 2021; **4**: 680–717.
- 8 Hori Y, Wakebe H, Tsukamoto T, *et al.* Electrocatalytic process of CO selectivity in electrochemical reduction of CO₂ at metal electrodes in aqueous media. *Electrochim Acta* 1994; **39**: 1833–1839.
- 9 Kuhl KP, Cave ER, Abram DN, *et al.* New insights into the electrochemical reduction of carbon dioxide on metallic copper surfaces. *Energy Environ Sci* 2012; **5**: 7050.
- 10 Gauthier JA, Lin Z, Head-Gordon M, *et al.* Pathways for the formation of C₂₊ products under alkaline conditions during the electrochemical reduction of CO₂. *ACS Energy Lett* 2022; **7**: 1679–1686.
- 11 Nitopi S, Bertheussen E, Scott SB, *et al.* Progress and perspectives of electrochemical CO₂ reduction on copper in aqueous electrolyte. *Chem Rev* 2019; **119**: 7610–7672.
- 12 Wu ZZ, Zhang XL, Niu ZZ, *et al.* Identification of Cu(100)/Cu(111) Interfaces as superior active sites for CO dimerization during CO₂ electroreduction. *J Am Chem Soc* 2022; **144**: 259–269.
- 13 Yang PP, Zhang XL, Gao FY, *et al.* Protecting copper oxidation state via intermediate confinement for selective CO₂ electroreduction to C₂₊ fuels. *J Am Chem Soc* 2020; **142**: 6400–6408.
- 14 Li F, Thevenon A, Rosas-Hernández A, *et al.* Molecular tuning of CO₂-to-ethylene conversion. *Nature* 2020; **577**: 509–513.
- 15 Li CW, Kanan MW. CO₂ reduction at low overpotential on Cu electrodes resulting from the reduction of thick Cu₂O films. *J Am Chem Soc* 2012; **134**: 7231–7234.
- 16 Li CW, Ciston J, Kanan MW. Electroreduction of carbon monoxide to liquid fuel on oxide-derived nanocrystalline copper. *Nature* 2014; **508**: 504–507.
- 17 Zhang B, Zhang J, Hua M, *et al.* Highly electrocatalytic ethylene production from CO₂ on nanodeficient Cu nanosheets. *J Am Chem Soc* 2020; **142**: 13606–13613.
- 18 Gu Z, Shen H, Chen Z, *et al.* Efficient electrocatalytic CO₂ reduction to C₂₊ alcohols at defect-site-rich Cu surface. *Joule* 2021; **5**: 429–440.
- 19 Verdager-Casadevall A, Li CW, Johansson TP, *et al.* Probing the active surface sites for CO reduction on oxide-derived copper electrocatalysts. *J Am Chem Soc* 2015; **137**: 9808–9811.
- 20 Sang J, Wei P, Liu T, *et al.* A Reconstructed Cu₂P₂O₇ Catalyst for Selective CO₂ Electroreduction to Multicarbon Products. *Angew Chem Int Ed* 2022; **61**: e202114238.
- 21 Lei Q, Zhu H, Song K, *et al.* Investigating the origin of enhanced C₂₊ selectivity in oxide-/hydroxide-derived copper electrodes during CO₂ electroreduction. *J Am Chem Soc* 2020; **142**: 4213–4222.
- 22 Lei Q, Huang L, Yin J, *et al.* Structural evolution and strain generation of derived-Cu catalysts during CO₂ electroreduction. *Nat Commun* 2022; **13**: 4857.
- 23 Brown Bourzutschky J. Conversion of synthesis gas over LaMn_{1-x}Cu_xO_{3+z}; perovskites and related copper catalysts. *J*

- Catal* 1990; **124**: 52–72.
- 24 Seitz LC, Dickens CF, Nishio K, *et al.* A highly active and stable $\text{IrO}_x/\text{SrIrO}_3$ catalyst for the oxygen evolution reaction. *Science* 2016; **353**: 1011–1014.
- 25 Schwartz M, Cook RL, Kehoe VM, *et al.* Carbon dioxide reduction to alcohols using perovskite-type electrocatalysts. *J Electrochem Soc* 1993; **140**: 614–618.
- 26 Mignard D, Barik RC, Bharadwaj AS, *et al.* Revisiting strontium-doped lanthanum cuprate perovskite for the electrochemical reduction of CO_2 . *J CO₂ Util* 2014; **5**: 53–59.
- 27 Cheong SW, Thompson JD, Fisk Z. Properties of La_2CuO_4 and related compounds. *Physica C-Supercond* 1989; **158**: 109–126.
- 28 Dwivedi A, Rodriguez MA, Cormack AN. Defect-chemical aspects in the synthesis of metallic conductors $\text{La}_{1-x}\text{Ba}_x\text{CuO}_3$ ($x = 0.0$ to 0.5). *J Am Ceramic Soc* 2005; **75**: 1993–1996.
- 29 Zheng K, Gorzkowska-Sobaś A, Świerczek K. Evaluation of Ln_2CuO_4 (Ln: La, Pr, Nd) oxides as cathode materials for IT-SOFCs. *Mater Res Bull* 2012; **47**: 4089–4095.
- 30 Gong Z, Zhong W, He Z, *et al.* Improving electrochemical nitrate reduction activity of layered perovskite oxide La_2CuO_4 via B-site doping. *Catal Today* 2022; **402**: 259–265.
- 31 Vasquez RP. X-ray photoemission measurements of $\text{La}_{1-x}\text{CaCoO}_3$ ($x=0, 0.5$). *Phys Rev B* 1996; **54**: 14938–14941.
- 32 Yousaf AB, Imran M, Farooq M, *et al.* Interfacial phenomenon and nanostructural enhancements in palladium loaded lanthanum hydroxide nanorods for heterogeneous catalytic applications. *Sci Rep* 2018; **8**: 4354.
- 33 Viswanathan B, Madhavan S, Swamy CS. Charge transfer satellites in X-ray photoelectron spectra of La_2CuO_4 . *Phys Stat Sol (B)* 1986; **133**: 629–632.
- 34 Imai Y, Kato M, Takarabe Y, *et al.* Low-temperature synthesis of La_2CuO_4 with the T'-structure from molten hydroxides. *Chem Mater* 2007; **19**: 3584–3585.
- 35 Whittingham AWH, Smith RDL. Electrochemically induced phase changes in La_2CuO_4 during cathodic electrocatalysis. *ChemElectroChem* 2019; **6**: 5116–5123.
- 36 Bard AJ, Parsons R, Jordan J. *Standard Potentials in Aqueous Solutions*. New York: Marcel Dekker, 1985.
- 37 Branco JB, Ballivet-Tkatchenko D, Matos AP. Reduction and catalytic behaviour of heterobimetallic copper-lanthanide oxides. *J Alloys Compd* 2008; **464**: 399–406.
- 38 Ciavatta L, Ferri D, Grenthe I, *et al.* Studies on metal carbonate equilibria. 3. The lanthanum(III) carbonate complexes in aqueous perchlorate media. *Acta Chem Scand* 1981; **35a**: 403–413.
- 39 Mariano RG, McKelvey K, White HS, *et al.* Selective increase in CO_2 electroreduction activity at grain-boundary surface terminations. *Science* 2017; **358**: 1187–1192.
- 40 Mariano RG, Kang M, Wahab OJ, *et al.* Microstructural origin of locally enhanced CO_2 electroreduction activity on gold. *Nat Mater* 2021; **20**: 1000–1006.
- 41 Sebastián-Pascual P, Escudero-Escribano M. Surface characterization of copper electrocatalysts by lead underpotential deposition. *J Electroanal Chem* 2021; **896**: 115446.
- 42 Rabinowitz JA, Kanan MW. The future of low-temperature carbon dioxide electrolysis depends on solving one basic problem. *Nat Commun* 2020; **11**: 5231.
- 43 Lv JJ, Jouny M, Luc W, *et al.* A highly porous copper electrocatalyst for carbon dioxide reduction. *Adv Mater* 2018; **30**: 1803111.
- 44 Zhang X, Li J, Li YY, *et al.* Selective and high current CO_2 electro-reduction to multicarbon products in near-neutral KCl electrolytes. *J Am Chem Soc* 2021; **143**: 3245–3255.
- 45 Ooka H, Figueiredo MC, Koper MTM. Competition between hydrogen evolution and carbon dioxide reduction on copper electrodes in mildly acidic media. *Langmuir* 2017; **33**: 9307–9313.
- 46 Ma M, Clark EL, Therkildsen KT, *et al.* Insights into the carbon balance for CO_2 electroreduction on Cu using gas diffusion electrode reactor designs. *Energy Environ Sci* 2020; **13**: 977–985.
- 47 Chen C, Yan X, Wu Y, *et al.* The *in situ* study of surface species and structures of oxide-derived copper catalysts for

- electrochemical CO₂ reduction. *Chem Sci* 2021; **12**: 5938–5943.
- 48 Yan X, Chen C, Wu Y, *et al.* Efficient electroreduction of CO₂ to C₂₊ products on CeO₂ modified CuO. *Chem Sci* 2021; **12**: 6638–6645.
- 49 Niu ZZ, Gao FY, Zhang XL, *et al.* Hierarchical copper with inherent hydrophobicity mitigates electrode flooding for high-rate CO₂ electroreduction to multicarbon products. *J Am Chem Soc* 2021; **143**: 8011–8021.
- 50 Endrödi B, Kecsenovity E, Samu A, *et al.* Multilayer electrolyzer stack converts carbon dioxide to gas products at high pressure with high efficiency. *ACS Energy Lett* 2019; **4**: 1770–1777.
- 51 Verma S, Hamasaki Y, Kim C, *et al.* Insights into the low overpotential electroreduction of CO₂ to CO on a supported gold catalyst in an alkaline flow electrolyzer. *ACS Energy Lett* 2017; **3**: 193–198.
- 52 Dinh CT, Burdyny T, Kibria MG, *et al.* CO₂ electroreduction to ethylene via hydroxide-mediated copper catalysis at an abrupt interface. *Science* 2018; **360**: 783–787.
- 53 Gunathunge CM, Li J, Li X, *et al.* Surface-adsorbed CO as an infrared probe of electrocatalytic interfaces. *ACS Catal* 2020; **10**: 11700–11711.
- 54 Li J, Chang X, Zhang H, *et al.* Electrokinetic and *in situ* spectroscopic investigations of CO electrochemical reduction on copper. *Nat Commun* 2021; **12**: 3264.
- 55 Gunathunge CM, Ovalle VJ, Li Y, *et al.* Existence of an electrochemically inert CO population on Cu electrodes in alkaline pH. *ACS Catal* 2018; **8**: 7507–7516.
- 56 Bai H, Cheng T, Li S, *et al.* Controllable CO adsorption determines ethylene and methane productions from CO₂ electroreduction. *Sci Bull* 2021; **66**: 62–68.
- 57 Chen S, Su Y, Deng P, *et al.* Highly selective carbon dioxide electroreduction on structure-evolved copper perovskite oxide toward methane production. *ACS Catal* 2020; **10**: 4640–4646.
- 58 Gunathunge CM, Li X, Li J, *et al.* Spectroscopic observation of reversible surface reconstruction of copper electrodes under CO₂ reduction. *J Phys Chem C* 2017; **121**: 12337–12344.
- 59 Smoluchowski R. Anisotropy of the electronic work function of metals. *Phys Rev* 1941; **60**: 661–674.
- 60 Mason SE, Grinberg I, Rappe AM. First-principles extrapolation method for accurate CO adsorption energies on metal surfaces. *Phys Rev B* 2004; **69**: 161401.
- 61 Vollmer S, Witte G, Wöll C. Determination of site specific adsorption energies of CO on copper. *Catal Lett* 2001; **77**: 97–101.
- 62 Liu X, Xiao J, Peng H, *et al.* Understanding trends in electrochemical carbon dioxide reduction rates. *Nat Commun* 2017; **8**: 15438.